

hep-ph/0005259
 FTUV/000522
 IFIC/00-26

The Simplest Resonant Spin–Flavour Solution to the Solar Neutrino Problem

O. G. Miranda ^b¹ C. Peña-Garay ^a, ² T. I. Rashba ^c, ³ V. B. Semikoz ^{a,c}, ⁴
 and J. W. F. Valle ^a⁵

^a *Instituto de Física Corpuscular - C.S.I.C./Universitat de València
 Edificio Institutos de Paterna, Apartado de Correos 2085
 46071 València, SPAIN
<http://neutrinos.uv.es>*

^b *Departamento de Física
 CINVESTAV-IPN, A. P. 14-740, México 07000, D. F., México.*

^c *The Institute of the Terrestrial Magnetism,
 the Ionosphere and Radio Wave Propagation of the Russian Academy of Science,
 IZMIRAN, Troitsk, Moscow region, 142092, Russia*

Abstract

We re-analyse the resonant spin–flavour (RSF) solutions to the solar neutrino problem in the framework of analytic solutions to the solar magneto-hydrodynamics (MHD) equations. By substantially eliminating the arbitrariness associated to the magnetic field profile due to both mathematical consistency and physical requirements we propose the simplest scheme (MHD-RSF, for short) for solar neutrino conversion using realistic static MHD solutions. Using such effective two-parameter scheme we perform the first global fit of the recent solar neutrino data, including event rates as well as zenith angle distributions and recoil electron spectra induced by solar neutrino interactions in Superkamiokande. We compare quantitatively our simplest MHD-RSF fit with vacuum oscillation (VAC) and MSW–type (SMA, LMA and LOW) solutions to the solar neutrino problem using a common

¹ E-mail: omr@fis.cinvestav.mx

² E-mail: penya@flamenco.ific.uv.es

³ E-mail: rashba@izmiran.rssi.ru

⁴ E-mail: semikoz@flamenco.ific.uv.es

⁵ E-mail: valle@flamenco.ific.uv.es

well-calibrated theoretical calculation and fit procedure. We find our MHD-RSF fit to be somewhat better than those obtained for the favored neutrino oscillation solutions, though not in a statistically significant way. We briefly discuss the prospects to disentangle our MHD-RSF scenario at future solar neutrino experiments, giving some predictions for the SNO experiment.

1 Introduction

The persistent disagreement between solar neutrino data and theoretical expectations has been a long-standing problem in physics. Since the very first measurements [1], the Solar neutrino problem has remained as a puzzle, re-confirmed by new data on rates by GALLEX-SAGE [2, 3] as well as most recently published 825–day data collected by the Super-Kamiokande collaboration [4] which goes beyond the simple rate measurements to include also rate-independent data such as the recoil electron spectra induced by solar neutrino interactions, as well as the zenith angle distributions [5]. It has often been argued that these data can not be accounted for by astrophysics [6]. Together with the atmospheric neutrino data [7] these constitute the only present-day evidence in favour of physics beyond the Standard Model, providing a strong hint for neutrino conversion.

The most popular solutions of the solar neutrino anomalies are based on the idea of neutrino oscillations, either in vacuum or in the Sun due to the enhancement arising from matter effects [8].

Although these are the simplest neutrino conversion mechanisms there is considerable interest in alternative interpretations. For example it has long been noted [9] that Majorana neutrinos may have non-zero transition magnetic moments which can generate spin-flavour conversions in the presence of a magnetic field. These are especially interesting for two reasons: (i) on general grounds [10] neutrinos are expected to be Majorana particles and (ii) conversions induced by transition magnetic moments can be resonant in the Sun [11]. There is also room for more exotic mechanisms such as flavour changing neutrino interactions [12] which do not require neutrino mass [13].

Here we will re-analyse the status of resonant spin-flavour solutions to the solar neutrino problem in the light of the most recent global set of solar neutrino data, including event rates as well as zenith angle distributions and recoil electron spectra induced by solar neutrino interactions in Superkamiokande which has attracted interest recently [14, 15]. In contrast to previous attempts we will adopt the general framework of self-consistent magneto-hydrodynamic (MHD) models of the Sun [16]. For definiteness we will concentrate in the recent proposal of Ref. [17] where relatively simple analytic solutions have been given. We perform global fits of solar neutrino data for realistic solutions to the magneto-hydrodynamics equations inside the Sun. This requires adjusting both the neutrino parameters as well as optimizing the magnetic field profile. The arbitrariness associated to the latter is substantially reduced due to mathematics (they must be solutions of MHD equations) as well as reasonable physical requirements. This

way and by neglecting neutrino mixing we obtain the simplest MHD-RSF solution to the solar neutrino problem, characterized by two effective parameters, Δm^2 and $\mu_\nu B_{\perp max}$, $B_{\perp max}$ being the maximum magnitude of the magnetic field inside the convective region. Throughout this paper we have assumed that the neutrino transition magnetic moment μ_ν is given in units of $\mu_{11} \equiv \mu_\nu/10^{-11} \mu_B$, where μ_B is the Bohr magneton and we set $\mu_{11} \equiv 1$ everywhere. Our MHD-RSF solution can be meaningfully compared with the neutrino oscillation solutions to the solar neutrino problem. We find that our simplest two-parameter MHD-RSF fits to the solar neutrino data are slightly better than those for the oscillation solutions, but not in a statistically significant way. The required best fit points correspond to maximum magnetic field magnitudes in the convective zone smaller than 100 KG. We briefly discuss the prospects to distinguish our simplest MHD-RSF scenario from the neutrino oscillation solutions to the solar neutrino problem at future solar neutrino experiments, giving some predictions for the SNO experiment.

2 Static Magnetic Field Profiles in the Sun

In solar magneto-hydrodynamics [18] (MHD, for short) one can explain the origin of solar magnetic fields from the dynamo mechanism at the bottom of the convective zone or, to be more specific, in the overshoot layer, where magnetic fields may be as strong as 300 kG [19]. Such a picture is quite attractive and several MHD dynamo solutions has been known since long time ago (see for example [16]) However the corresponding magnetic field profiles are rather complicated and difficult to extract. For this reason there have been many attempts to mimic MHD properties through the use of *ad hoc* magnetic field profiles involving, for example, twisting fields [20].

Here we will follow an alternative approach using fully self-consistent solutions to the MHD equations inside the Sun. To achieve this we focus on the case of stationary solutions which are known analytically in terms of relatively simple functions [17]. This way we obtain a simple and well-motivated magnetic field profile, without the full complexity that a dynamo model implies. In this section we will explain this model and discuss the limits on the shape parameters describing the field profile. We will also discuss how to relate this model with the dynamo picture of the solar interior.

2.1 Single-Mode Field Configurations

In this subsection we will describe the model that we are using for the magnetic field profile. We consider only solutions to the equation for a static MHD plasma configuration

in a gravitational field, given by

$$\nabla p - \frac{1}{c} \vec{j} \times \vec{B} + \rho \nabla \Phi = 0. \quad (1)$$

This static MHD equations correspond to a quiet Sun and they admit axially symmetric solutions in the spherically symmetric gravitational field which can be simply expressed in terms of spherical Bessel functions and were first discussed in Ref. [17]. For this model the magnetic field will be given by a family of solutions that depends on z_k , the roots of the spherical Bessel function $f_{5/2} = \sqrt{z} J_{5/2}(z)$, to ensure the boundary condition that \vec{B} vanishes on the solar surface. Within the solar interior the magnetic field for any k will be then given by

$$\begin{aligned} B_r^k(r, \theta) &= 2\hat{B}^k \cos \theta \left[1 - \frac{3}{r^2 z_k \sin z_k} \left(\frac{\sin(z_k r)}{z_k r} - \cos(z_k r) \right) \right] , \\ B_\theta^k(r, \theta) &= -\hat{B}^k \sin \theta \left[2 + \frac{3}{r^2 z_k \sin z_k} \left(\frac{\sin(z_k r)}{z_k r} - \cos(z_k r) - z_k r \sin(z_k r) \right) \right] , \\ B_\phi^k(r, \theta) &= \hat{B}^k z_k \sin \theta \left[r - \frac{3}{r z_k \sin z_k} \left(\frac{\sin(z_k r)}{z_k r} - \cos(z_k r) \right) \right] , \end{aligned} \quad (2)$$

where the coefficient $\hat{B}^k(B_{core})$ is given by

$$\hat{B}^k = \frac{B_{core}}{2(1 - z_k / \sin z_k)} . \quad (3)$$

Here θ is the polar angle and the distance r has been normalized to $R_\odot = 1$. Taking into account the inclination of the solar equator to the ecliptics, where neutrinos propagate to the Earth, it follows that θ lies in the narrow range $83^\circ - 97^\circ$, depending on the season. In our calculations we have averaged over θ in the above range.

The modulus of the perpendicular component which is relevant to the neutrino spin-flavour takes the form

$$B_\perp = \sqrt{B_\phi^2 + B_\theta^2} = B_{core} \frac{\sin \theta}{r} f(r) , \quad (4)$$

where $f(r)$ is some known smooth function. Notice also that the behaviour of \mathbf{B} at the solar center ($r = 0$)

$$\begin{aligned} B_r(0, \theta) &= B_{core} \cos \theta , \\ B_\theta(0, \theta) &= -B_{core} \sin \theta , \\ B_\phi(0, \theta) &= B_{core} \sin \theta \frac{z_k}{2} \frac{r}{R_\odot} \rightarrow 0 , \end{aligned} \quad (5)$$

is completely regular, determined only by the parameter B_{core} . In Fig. 1 we display the perpendicular component of \mathbf{B} for various k -values 1, 3 and 10, which correspond to the roots $z_k = 5.7$, $z_k = 12.3$ and $z_k = 34.5$, respectively.

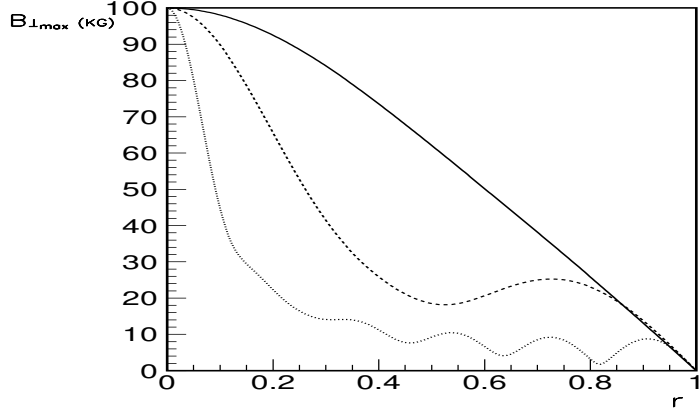


Figure 1: The perpendicular component of \mathbf{B} for various k -values 1 (solid), 3 (dashed) and 10 (dotted).

2.2 Astrophysical Constraints on Magnetic Fields

We now discuss the astrophysical restrictions on the free parameters B_{core} and k characterizing the model. We can see that the magnitude of a magnetic field at the center of the Sun is constrained by the Fermi-Chandrasekhar limit [21] which implies [17]

$$\eta = \frac{2}{15} \frac{5\gamma_0 - 6}{\gamma_0 - 1} \frac{(\hat{B}^k)^2 z_{2k}^2 R_\odot^4}{GM_\odot^2} \lesssim 1, \quad (6)$$

here γ_0 is polytropic index characterizing the equation of state (pressure $P \sim \rho_0^\gamma$), M_\odot is the solar mass and G is Newton's constant. This equation gives us an upper bound on $B_{core} \lesssim 2$ MGauss for $k = 1$. For higher values of k this constraint is even weaker.

Regarding with the values of k . These can be constrained by taking into account that in order to justify the use of a stationary solution, it is necessary that the diffusion time due to ohmic dissipation

$$t_{diss}(k) = \frac{4\pi\sigma_{cond}L^2(k)}{c^2} \quad (7)$$

must be bigger than the age of the Sun $t_\odot \simeq 1.4 \times 10^{17} s$ [22]. Here $L(k)$ denotes a characteristic spatial scale of the magnetic field. As we can see from Fig. 1 $L(k=1) \sim R_\odot$, while $L(k) \simeq R_\odot/k$. In eq. (7) $\sigma_{cond} = \omega_p^2/(4\pi\nu_{ep})$ denotes the conductivity of the fully ionized hydrogen plasma. After substituting the plasma frequency

$$\omega_p = 5.65 \times 10^4 \sqrt{\frac{n_e}{1cm^{-3}}} s^{-1}$$

and the e - p collision frequency

$$\nu_{ep} = 50 \left(\frac{n_e}{1cm^{-3}} \right) \left(\frac{T}{1K} \right)^{-3/2} s^{-1}$$

we obtain from eq. (7) an estimate of the magnetic field dissipation time $t_{diss}(k)$

$$t_{diss}(k) = \frac{6.4 \times 10^7 R_\odot^2 1/s}{c^2} \times \frac{(T/K)^{3/2}}{k^2} > t_\odot \quad (8)$$

Note that the dissipation time is shorter for higher k values, long-lived field configurations being possible only if k is small. For example, the dissipation time for the third mode is about an order magnitude less than that for the first mode. Moreover it depends on the value of the temperature that we take. Some typical values for the temperature are $T_{\min} \simeq 2.8 \times 10^5 K$ for the bottom of the convective zone and $T_{\max} \simeq 1.6 \times 10^7 K$ for the solar core [23]. Thus, taking the optimistic estimate, T_{\max} , we obtain $k < k_M = 13$, while, if we consider the average value $T = 4 \times 10^6 K$ we will have $k < k_M = 5$. In what follows we will consider values of $k \leq 10$.

2.3 Energy localization criterium

It is commonly accepted that magnetic fields measured at the surface of the Sun are weaker than within the convective zone interior where this field is supposed to be generated. It is known by observational data that the mean field value over the solar disk is of the order of 1 Gauss while in the solar spots magnetic field strength reaches 1 KG.

On the other hand the general knowledge of the solar magnetic field models is that the magnetic field increases at the overshoot layer, while being small at the solar interior, a picture rather opposite to the one we have seen in Fig. 1.

This conflict can be avoided by taking advantage of the linear nature of the basic equilibrium MHD equation in eq. (1). This implies that any linear combination of solutions \vec{B}^k ($k = 1, 2, \dots, k_M$, for some fixed number k_M)

$$\vec{B} = c_1 \vec{B}_1 + c_2 \vec{B}_2 + \dots + c_M \vec{B}_M \quad (9)$$

is also a solution. As mentioned in section 2.2 we will adopt $k_M \leq 10$ in order to ensure that ohmic dissipation is acceptable and therefore justify the static approximation.

In order to ensure that the magnetic field energy is localized mainly within the convective region we will now supplement the constraints of section 2.2 by imposing that the magnetic field should vanish in the center of the Sun

$$\vec{B}(\vec{r} = 0) = 0 \quad (10)$$

The latter implies

$$c_1 + c_2 + \dots + c_{k_M} = 0. \quad (11)$$

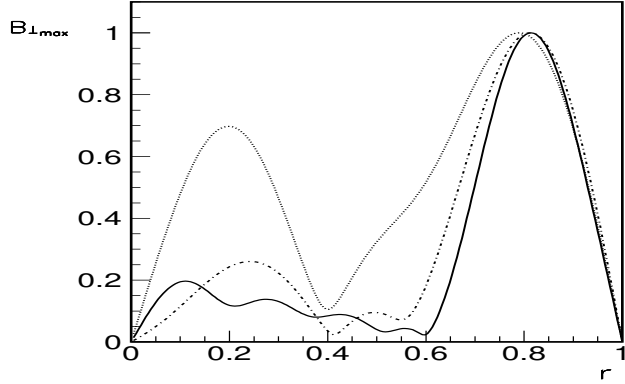


Figure 2: Magnetic field configurations obtained by combining individual modes for different k_M values, 5, 6 and 10. Summing up to higher modes achieves better localization of the field in the convective region (solid).

Therefore we will have, in principle, $k_M - 1$ free parameters.

We will require, in addition, that the magnetic field energy must be minimal in the region below the bottom of the convective zone, characterized by a certain value of r_0

$$E_B = \int_0^{r_0} d^3r \frac{\vec{B}^2(r)}{8\pi} . \quad (12)$$

This implies

$$\frac{\partial}{\partial c_i} E_B \equiv \sum_{j=1}^{k_M-1} c_j a_{ij} = 0 \quad (13)$$

where

$$a_{ij} = \int_0^{r_0} d^3r (\vec{B}^j - \vec{B}^M) \cdot \vec{B}^i . \quad (14)$$

Without loss of generality we can assume that one of the coefficients is non-zero, which prevents us from having only the trivial solution $c_i \equiv 0$. Taking $c_{k_M-1} \neq 0$ we will have the linear non-homogeneous equation

$$\sum_{j=1}^{M-2} c_j a_{ij} = -c_{k_M-1} a_{ik_{M-1}} \quad (15)$$

which determines all the c_i coefficients in terms of, say, c_{k_M-1} . As expected on physical grounds, this last remaining parameter c_{k_M-1} corresponds to the maximum magnetic field magnitude in the convective region, i.e. $B_{\perp_{max}}$ is proportional to c_{k_M-1} .

The procedure sketched above provides a consistent method for combining individual mode solutions \vec{B}_k of the static MHD equation, while fixing all of the coefficients of the linear combination, leaving as free parameters only the value of $B_{\perp_{max}}$ inside the convective region and the value of $k_M \leq 10$. In Fig. (2) we show the resulting profiles

for $k_M = 5, 6, 10$. The parameter r_0 could also be taken as a free parameter but, on physical grounds, it should lie in a narrow range close to overshoot layer. We show explicitly that varying r_0 has little effect on our results.

3 Fitting the Solar Neutrino Data

The neutrino evolution Hamiltonian in a magnetic field is well-known to be four-dimensional [9]. For definiteness and simplicity we will neglect neutrino mixing in what follows and consider the case of active-active neutrino conversions. This will allow us to compare our χ^2 -analysis with the previous ones [14, 15]. The $\nu_e \rightarrow \bar{\nu}_\ell$ conversions are described by the master Schrödinger evolution equation

$$i \begin{pmatrix} \dot{\nu}_e \\ \dot{\bar{\nu}}_\ell \end{pmatrix} = \begin{pmatrix} V_e - \delta & \mu_\nu B_+ \\ \mu_\nu B_- & -V_\ell + \delta \end{pmatrix} \begin{pmatrix} \nu_e \\ \bar{\nu}_\ell \end{pmatrix}, \quad (16)$$

where μ_ν denotes the neutrino transition magnetic moment [9] in units of $10^{-11} \mu_B$, ℓ denoting either μ or τ . Here $B_\pm = B_x \pm iB_y$ and $\delta = \Delta m^2/4E$ is the neutrino mass parameter; $V_e(t) = G_F \sqrt{2}(\rho(t)/m_p)(Y_e - Y_n/2)$ and $V_\ell(t) = G_F \sqrt{2}(\rho(t)/m_p)(-Y_n/2)$ are the neutrino vector potentials for ν_e and ν_ℓ in the Sun given by the abundances of the electron ($Y_e = m_p N_e(t)/\rho(t)$) and neutron ($Y_n = m_p N_n(t)/\rho(t)$) components. In our numerical study of solar neutrino data we adopt the Standard Solar Model density profile of ref.[23].

We solve Eq. (16) numerically by finding a solution of the Cauchy problem in the form of a set of wave functions $\nu_a(t) = |\nu_a(t)| e^{i\Phi_a(t)}$ from which the neutrino survival probabilities $P_{aa}(t) = \nu_a^* \nu_a$ are calculated. They obey the unitarity condition $\sum_a P_{aa} = 1$ where the subscript a denotes $a = e$ for ν_e and $a = \ell$ for $\bar{\nu}_\ell$ respectively.

As an illustration we display in Fig. (3) the electron neutrino survival probability P_{ee} calculated in the MHD-RSF scheme from eq. (16) plotted versus $E/\Delta m^2$. This is obtained with the magnetic field configurations given in Fig. (2).

We will now re-analyse the status of resonant spin-flavour solutions to the solar neutrino problem in the light of the most recent global set of solar neutrino data, including event rates as well as zenith angle distributions and recoil electron spectra induced by solar neutrino interactions in Superkamiokande which has attracted interest recently [14, 15]. It has been found that the quality of the fit to the solar neutrino data depends on the magnetic field profile. The best solutions have been obtained with a magnetic field around 100 KG in the convective zone and zero at the core (profiles 3 and

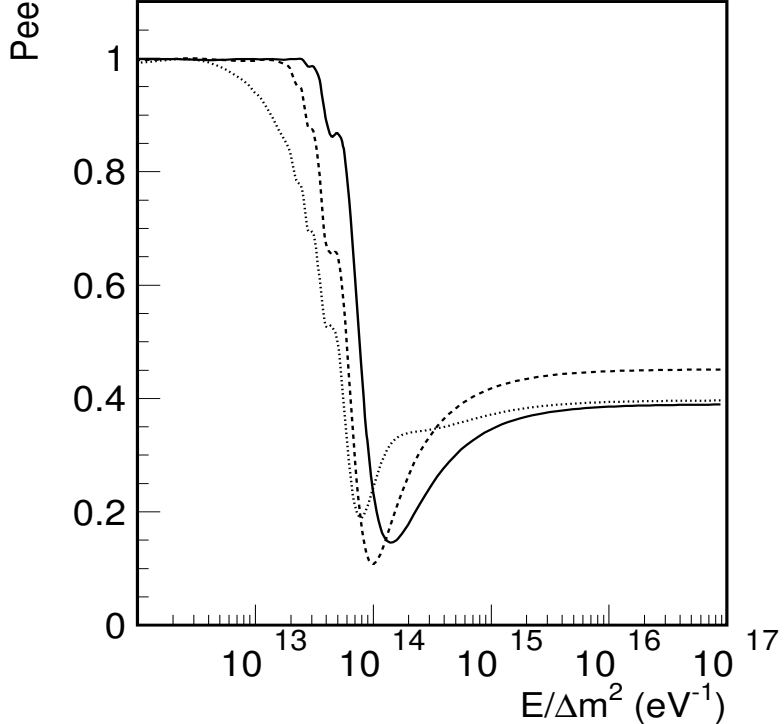


Figure 3: Typical MHD-RSF neutrino survival probability P_{ee} versus $E/\Delta m^2$.

6 of first and second paper in Ref [14], respectively) or an almost constant magnitude of the magnetic field, but with twisting direction [15] using the profiles given in [20].

In contrast with previous work we will consider the fits obtained when we employ self-consistent solutions of MHD equations which obey the physical requirements we derived in sec. 2.2 using the procedure for combining magnetic field modes described in section 3. Our approach is *global* and allows us to compare quantitatively with other solutions to the solar neutrino problem within the same well calibrated theoretical calculation and fit procedure.

3.1 Rates

In order to determine the possible values of the parameters characterizing the MHD-RSF solution to the solar neutrino problem, we have first used the data on the total event rates measured at the Chlorine experiment in Homestake [1], at the two Gallium experiments GALLEX and SAGE [2, 3] and the 825-day Super-Kamiokande data sample, as given in table 1.

In our statistical treatment of the data for the combined fit we adopt the χ^2 definition

| Experiment | Rate | Ref. | Units | R_i^{BP98} |
|------------------|-----------------|--------|---------------------------------------|---------------------|
| Homestake | 2.56 ± 0.23 | [1] | SNU | 7.8 ± 1.1 |
| GALLEX + SAGE | 72.3 ± 5.6 | [2, 3] | SNU | 130 ± 7 |
| Super-Kamiokande | 2.45 ± 0.08 | [4] | $10^6 \text{ cm}^{-2} \text{ s}^{-1}$ | 5.2 ± 0.9 |

Table 1: Solar neutrino rates measured in the Chlorine, Gallium and Super-Kamiokande experiments.

given in ref. [24],

$$\chi^2_R = \sum_{i,j=1,3} (R_i^{\text{th}} - R_i^{\text{exp}}) , \sigma_{ij}^{-2} (R_j^{\text{th}} - R_j^{\text{exp}}) \quad (17)$$

where R_i^{th} is the theoretical prediction of the event rate in detector i and R_i^{exp} is the measured rate. The error matrix σ_{ij} contains not only the theoretical uncertainties but also the experimental errors, both systematic and statistical.

The general expression of the expected event rate in the presence of oscillations in experiment i is given by R_i^{th}

$$R_i^{\text{th}} = \sum_{k=1,8} \phi_k \int dE_\nu \lambda_k(E_\nu) \times [\sigma_{e,i}(E_\nu) \langle P_{ee}(E_\nu, t) \rangle + \sigma_{x,i}(E_\nu) (1 - \langle P_{ee}(E_\nu, t) \rangle)], \quad (18)$$

where E_ν is the neutrino energy, ϕ_k is the total neutrino flux and λ_k is the neutrino energy spectrum (normalized to 1) from the solar nuclear reaction k [25] with the normalization given in Ref. [23]. Here $\sigma_{e,i}$ ($\sigma_{x,i}$) is the ν_e (ν_x) (with x being $\bar{\mu}$ or s corresponding to active-active or active-sterile MHD-RSF conversions) cross section in the Standard Model [26] with the target corresponding to experiment i , and $\langle P_{ee}(E_\nu, t) \rangle$ is the time-averaged ν_e survival probability.

For the Chlorine and Gallium experiments we use improved cross sections $\sigma_i(E)$ from Ref. [27]. For the Super-Kamiokande experiment we calculate the expected signal with the corrected cross section given in the Appendix Sec. A.

The expected signal in the absence of oscillations, R_i^{BP98} , can be obtained from Eq.(18) by substituting $P_{ee} = 1$. In table 1 we also give the expected rates at the different experiments which we obtain using the fluxes of Ref. [23].

In Fig. (4) we display the region of MHD-RSF parameters allowed by the solar neutrino rates.

Our χ^2 analysis of the solar neutrino rates uses the magnetic field profiles discussed in Sections 2 and 3. As we mentioned in that section, these profiles are characterized by

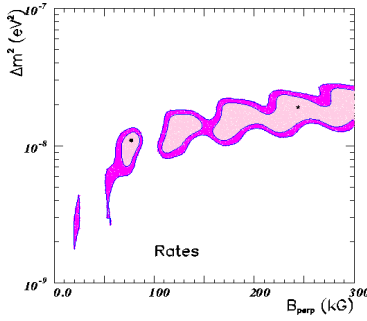


Figure 4: MHD-RSF 90% CL (light) and 99% CL (dark) regions of Δm^2 versus $B_{\perp max}(KG)$ allowed by the rates given in table 1, for $r_0 = 0.6$ and $K_M = 6$

k_M and r_0 . In table 2 we present the best fit points for k_M from 4 to 8 and for $r_0 \simeq .6R\odot$ and for $B_{\perp max} < 300$ KGauss. In the same table we also show the best fit points for $B_{\perp max} < 100$ KGauss. We can see from this table that the χ^2 is pretty stable and does not depend significantly on the choice of k_M and r_0 allowed by astrophysics. In Fig. (4) we display the region of MHD-RSF parameters allowed by the solar neutrino rates for the case $M = 6$ and $r_0 = .6R\odot$. We can see that there are several allowed regions for different values of the magnetic field. As we already mentioned, in our analysis we have fixed the value of μ_ν to be $10^{-11}\mu_B$. Since evolution equation depends on the product $\mu_\nu B$, a smaller value of the neutrino magnetic moment the $B_{\perp max}$ axis in Fig. (4) must be rescaled. In this sense, the local minima shown in table 2 for $B_{\perp max} < 100$ KGauss allows a smaller μ_ν .

3.2 Zenith and Spectrum Fit

Apart from total event rates the water Cerenkov experiment also measures the zenith angle distribution of solar neutrino events as well as their electron recoil energy spectrum with their recent 825-day data sample [4].

The smallness of the Δm^2 values indicated by the rates fit implies that no appreciable day–night variation of the counting rates is expected in our MHD-RSF solution. However the measured solar neutrino zenith angle data must be included in the analysis and we do that. This is necessary in order to enable us a meaningful comparison with vacuum

| | | $0.6R_{\odot}$ | | | $0.62R_{\odot}$ | | | $0.64R_{\odot}$ | |
|-----|-----------------|----------------------|----------------|-----------------|----------------------|----------------|-----------------|----------------------|----------------|
| M | $B_{\perp max}$ | Δm^2 | χ^2_{min} | $B_{\perp max}$ | Δm^2 | χ^2_{min} | $B_{\perp max}$ | Δm^2 | χ^2_{min} |
| 4 | 29. | $.84 \times 10^{-8}$ | 1.3 | 32 | $.94 \times 10^{-8}$ | 1.1 | 41 | $.99 \times 10^{-8}$ | 1.3 |
| | 29. | $.84 \times 10^{-8}$ | 1.3 | 32 | $.94 \times 10^{-8}$ | 1.1 | 41 | $.99 \times 10^{-8}$ | 1.3 |
| 5 | 71 | 1.5×10^{-8} | 1.0 | 63 | 1.5×10^{-8} | .87 | 72 | 1.6×10^{-8} | .95 |
| | 71 | 1.5×10^{-8} | 1.0 | 63 | 1.5×10^{-8} | .87 | 72 | 1.6×10^{-8} | .95 |
| 6 | 244 | 1.9×10^{-8} | .03 | 247 | 1.9×10^{-8} | .06 | 251 | 1.9×10^{-8} | .13 |
| | 77 | 1.1×10^{-8} | .33 | 80 | 1.0×10^{-8} | .40 | 80 | 1.0×10^{-8} | .35 |
| 7 | 208 | 1.2×10^{-8} | .20 | 210 | 1.0×10^{-8} | .13 | 215 | $.94 \times 10^{-8}$ | .26 |
| | 83 | $.75 \times 10^{-8}$ | .52 | 84 | $.71 \times 10^{-8}$ | .54 | 84 | $.64 \times 10^{-8}$ | .47 |
| 8 | 220 | $.98 \times 10^{-8}$ | .38 | 222 | $.94 \times 10^{-8}$ | .24 | 225 | $.84 \times 10^{-8}$ | .45 |
| | 87 | $.64 \times 10^{-8}$ | .68 | 87 | $.59 \times 10^{-8}$ | .64 | 87 | $.55 \times 10^{-8}$ | .69 |

Table 2: Best fit points for the rates-only analysis for different r_0 and k_M values in active-active MHD-RSF oscillations.

and matter oscillations using the same statistical criteria [24, 28, 29], see definitions in the appendix. We obtain $\chi^2_{zenith} = 5.4$ for the full range of parameters in the analysis, the same as for the no-oscillation case.

The recoil electron energy spectrum induced by solar neutrino interactions after 504 days of operation is given for energies above 6.5 MeV using the Low Energy (LE) analysis in which the recoil energy spectrum is divided into 16 bins, 15 bins of 0.5 MeV energy width and the last bin containing all events with energy in the range 14 MeV to 20 MeV. Below 6.5 MeV the background of the LE analysis increases very fast as the energy decreases. Super-Kamiokande has designed a new Super Low Energy (SLE) analysis in order to reject this background more efficiently so as to be able to lower their threshold down to 5.5 MeV. In their 825-day data [4] they have used the SLE method and they present results for two additional bins with energies between 5.5 MeV and 6.5 MeV. In the appendix we present these data in table 7 as well as the details of our statistical analysis. Our results are almost independent of the choice of the parameters k_M and r_0 in the physical range, thus establishing the robustness of the fit procedure. The predicted spectrum is essentially flat except for the upper part of the Δm^2 region. As an example, we show in fig. 5 the excluded region at 99 % CL for the case $k_M = 6$ and $r_0 = 0.6$.

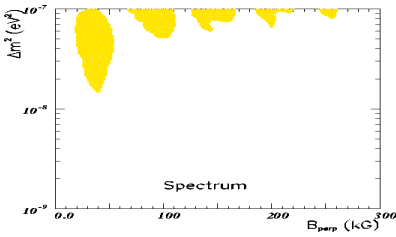


Figure 5: MHD-RSF 99% CL regions of Δm^2 versus $B_{\perp max}$ forbidden by the recoil electron spectrum data given in table 7 of the appendix, for $r_0 = 0.6$ and $k_M = 6$

3.3 Global Fit

As we have seen in the partial analysis, zenith and spectrum are essentially flat in the region of parameters which provide a good fit for the rates-only analysis. For this reason, the allowed regions are slightly modified by the inclusion of the zenith angular dependence and the energy spectrum data. As the results are statistically independent of the choice of k_M and r_0 in the physical range, our analysis effectively involves only two parameters. It is therefore meaningful to compare it with the popular two-neutrino fits characterizing vacuum or matter-enhanced oscillations. In table 3, we show the best-fit points in the range of our study for different k_M and r_0 values. Moreover, we show the local (global) minimum for $B_{\perp max}$ less than 100 KG, which will be important to improve sensitivity on the transition magnetic moment of the neutrino. In fig. 5 we show the allowed region at 90% CL and 99% CL for the case $r_0 = 0.6$ and $k_M = 6$. We have also investigated the effect of varying the hep flux, obtaining for the allowed regions results similar to the no-oscillation solution discussed previously in ref. [24], independently of the Δm^2 and $B_{\perp max}$ value, with a *hep* normalization factor of 13.5.

We now move to the case of active-sterile MHD-RSF conversions. The results given above for active-active MHD-RSF conversions change when conversions involve sterile neutrinos. The best fit points (and local ones) are obtained with parameters slightly modified with respect to those obtained for the active-active case. In the rates only fit, the χ^2_{rates} is worse than for the active-active case, essentially due to the neutral current

| | | $0.6R_\odot$ | | | $0.62R_\odot$ | |
|-----|-----------------|----------------------|----------------|-----------------|----------------------|----------------|
| M | $B_{\perp max}$ | Δm^2 | χ^2_{min} | $B_{\perp max}$ | Δm^2 | χ^2_{min} |
| 5 | 72 | 1.6×10^{-8} | 25.7 | 72. | 2.0×10^{-8} | 25.7 |
| | 72 | 1.6×10^{-8} | 25.7 | 72. | 2.0×10^{-8} | 25.7 |
| 6 | 240 | 1.8×10^{-8} | 24.7 | 241 | 1.8×10^{-8} | 24.9 |
| | 80 | 1.1×10^{-8} | 25.7 | 80 | 1.1×10^{-8} | 25.9 |

Table 3: Global best fit points and local minima for $B_{\perp max} < 100$ kGauss for different r_0 and k_M values in active-active MHD-RSF conversion scenario.

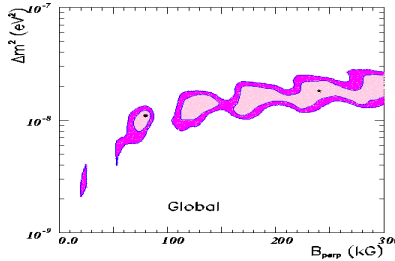


Figure 6: 90% CL (light) and 99% CL (dark) allowed MHD-RSF regions in Δm^2 and $B_{\perp max}$ from the measurements of rates combined with the zenith angle distribution and the recoil energy spectrum in super-Kamiokande, for $r_0 = 0.6$ and $k_M = 6$.

| | | $0.6R_\odot$ | | | $0.62R_\odot$ | |
|-----|-----------------|----------------------|----------------|-----------------|----------------------|----------------|
| M | $B_{\perp max}$ | Δm^2 | χ^2_{min} | $B_{\perp max}$ | Δm^2 | χ^2_{min} |
| 5 | 68. | 1.4×10^{-8} | 34.0 | 68 | 1.5×10^{-8} | 35.2 |
| | 68. | 1.4×10^{-8} | 34.0 | 68 | 1.5×10^{-8} | 35.2 |
| 6 | 247. | 1.9×10^{-8} | 28.7 | 247. | 1.9×10^{-8} | 28.2 |
| | 75. | 1.1×10^{-8} | 30.5 | 75. | 1.0×10^{-8} | 30.6 |

Table 4: Best fit points and local minima for $B_{\perp max} < 100kG$ for the global analysis for different r_0 and k_M values in active-sterile MHD-RSF conversions.

contribution in the Super-Kamiokande experiment. The zenith angle dependence and the recoil energy spectrum remains flat as before. The global fit for different r_0 and k_M , is shown in table 4.

4 MHD-RSF versus Oscillation Solutions

4.1 Present

From the results of the previous section it follows that our MHD-RSF solution to the solar neutrino problem provides a good description of the most recent solar neutrino data, including event rates as well as zenith angle distributions and recoil electron spectra induced by solar neutrino interactions in Superkamiokande. We have shown that our procedure is quite robust in the sense that the magnetic field profile has been determined in an essentially unique way. This effectively substitutes the neutrino mixing which characterizes the oscillation solutions by a single parameter $B_{\perp max}$ characterizing the maximum magnitude of the magnetic field inside the convective region. The value of k_M characterizing the maximum number of individual modes superimposed in order to obtain a realistic profile and the parameter r_0 characterizing the location of the convective region are severely restricted. The allowed k_M values are restricted by ohmic dissipation arguments to be lower than 10 or so, while r_0 is close to $0.6R_\odot$. We have found that our solar neutrino fits are pretty stable as long as k_M exceeds 5 and r_0 lies in the relevant narrow range (see tables 2 and 3). Therefore our fits are effectively two-parameter fits (Δm^2 and $B_{\perp max}$) whose quality can be meaningfully compared with that of the fits obtained for the favored neutrino oscillation solutions to the solar neutrino problem. In table 5 we compare the various solutions of the solar neutrino problem with the MHD-

| Solution | Δm^2 | $B_{\perp max}$ | χ^2_{min} (Prob %) | |
|---------------|-----------------------|----------------------|-----------------------------|-----------|
| $MHD - RSF_a$ | 1.1×10^{-8} | 80 | 25.7 (32) | this work |
| $MHD - RSF_s$ | 1.1×10^{-8} | 75 | 30.5 (14) | this work |
| | Δm^2 | $\sin^2(2\vartheta)$ | χ^2_{min} (Prob %) | Ref. |
| SMA_a | 5.2×10^{-6} | 4.7×10^{-3} | 29.7 (16) | [24, 28] |
| LMA | 2.4×10^{-5} | 0.78 | 27.0 (26) | [24, 28] |
| LOW | 1.0×10^{-7} | 0.93 | 32.0 (10) | [24, 28] |
| SMA_s | 5.2×10^{-6} | 4.7×10^{-3} | 32.0 (10) | [24, 29] |
| VAC | 4.4×10^{-10} | 0.9 | 34.3 (6) | [29] |
| no-osc | | | 87.9 (6×10^{-7}) | [24] |

Table 5: Best fit points and the corresponding probabilities for different solutions to the solar neutrino problem. The top row corresponds to the MHD-RSF solution presented here.

RSF solutions for the lower magnetic field presented here. Clearly the MHD-RSF fits seem somewhat better (though not in a statistically significant way) than those obtained for the MSW effect [24] as well as just-so solutions [29]. Notice that in table 5 we have used the same common calibrated theoretical procedures and statistical criteria. These results are for the case where the BP98 Standard Solar Model is adopted. We have also investigated the effect of varying the *hep* flux, obtaining a *hep* normalization factor of 13.5 to be compared with 12 for the SMA solution, 38 for the LMA solution and 15 for the VAC solution.

4.2 Future

Having performed our global analysis of the recent solar neutrino data within the framework of our MHD-RSF solution to the solar neutrino problem, we are in a position to calculate also the expected values of a number of observables to be measured by future solar neutrino experiments, such as SNO or Borexino. This task has been developed for the case of oscillation-type solutions to the solar neutrino problem in ref. [30]. Here we will consider our alternative MHD-RSF solution described in sections 2 and 3, because of its theoretical elegance and the good quality of the global fits it provides. Again, the results of refs. [24, 28, 29] will allow us to compare quantitatively our simplest MHD-RSF predictions with those associated with the vacuum (VAC) and MSW-type (SMA,

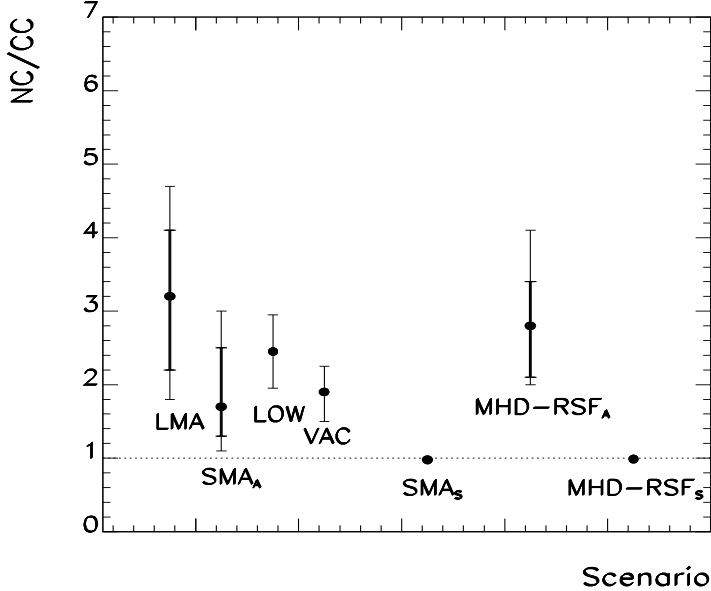


Figure 7: Neutral-to-charged-current event ratio expected at SNO for different solutions to the solar neutrino problem at 90% CL and 99% CL. The no-oscillation or SM case is denoted by the horizontal line at one.

LMA and LOW) solutions to the solar neutrino problem using the same well-calibrated theoretical calculation and fit procedure.

We determine the expected solar neutrino rates at SNO using the cross sections of the CC and NC νd reactions given by ref. [31] and the best-fit points we have determined in the present paper. For definiteness we have considered the global best fit points and local minima for $B_{\perp max} < 100kG$ given in table 3, for the case $k_M = 6$ and $r_0 = 0.6$ and active-active MHD-RSF conversions.

We have calculated the neutral-to-charged-current event ratio (NC/CC for short) and our results are presented in Fig. (7). Our predictions for the oscillation solutions agree relatively well with those of [30]. The agreement is not perfect because we use the full zenith angle dependence in the analysis of the solar neutrino data instead of simply the day-night asymmetry employed in ref. [30].

Clearly from Fig. (7) we see that there is a substantial overlap between our MHD-RSF predictions and those found for each of the oscillation solutions (SMA, LMA, LOW, VAC). The overlap is especially large between the LMA and the MHD-RSF solutions. Taking into account the present theoretical uncertainties and a reasonable estimate of the experimental errors attainable, it follows that an unambiguous discrimination between our MHD-RSF solution and the neutrino oscillation-type solutions to the solar neutrino

problem on the basis of the averaged event rates seems rather difficult. The expected features of the MHD-RSF recoil electron spectrum will be discussed elsewhere [32].

5 Discussion & Conclusions

We have re-analysed the status of resonant spin-flavour solutions to the solar neutrino problem in the framework of analytic solutions to the solar magneto-hydrodynamics equations, using the most recent global set of solar neutrino data. We have shown that our procedure is quite robust in the sense that the arbitrariness associated to the magnetic field profile has been almost eliminated due to both mathematical consistency and physical requirements. Effectively our analysis substitutes neutrino mixing by a single parameter $B_{\perp max}$ characterizing the maximum magnitude of the magnetic field inside the convective region. The value of k_M characterizing the maximum number of individual modes combined in a realistic profile and the parameter r_0 characterizing the location of the convective region are severely restricted. The allowed k_M values are restricted by ohmic dissipation arguments to be lower than 10 or so, and we have found that our solar neutrino fits are pretty stable as long as k_M exceeds 5. Moreover our fits are pretty stable within the relevant narrow range for r_0 . This way we obtain effective two-parameter global fits of solar neutrino data for static MHD solutions characterized by Δm^2 and $B_{\perp max}$, since the magnetic field profile is essentially unique. This enables us to compare their quality with that of the fits obtained for the favored neutrino oscillation solutions to the solar neutrino problem. Adopting the Standard Solar Model we have found the MHD-RSF fits to be slightly better than the oscillation fits, though not in a statistically significant way. We have also analysed the prospects to distinguish our best MHD-RSF solution from the oscillation solutions (SMA, LMA, LOW, VAC) at future solar neutrino experiments. Both in the comparison of the present status of different solutions of the solar neutrino problem, as well as in their future predictions at SNO we have used a common well-calibrated theoretical procedure and statistical criteria. Taking into account the present theoretical uncertainties and the expected experimental errors attainable, an unambiguous discrimination between our MHD-RSF solution and the neutrino oscillation-type solutions to the solar neutrino problem at the SNO experiment seems rather difficult. On the other hand better measurements of rate-independent solar neutrino observables such as the day-night asymmetry and seasonality would be potentially useful, since our MHD-RSF predictions differ from the expectations of the oscillation schemes. For example, seasonality is expected to be smaller [32] in our MHD-

RSF solution than in MSW [33] or just-so oscillations [29]. On the other hand the day-night asymmetry of the MHD-RSF solution is negligible, in contrast with the MSW solutions [32].

Note, however, that the *complete* MHD-RSF solution is characterized also by a non-zero neutrino flavour mixing. This gives it the potential to be discriminated from the oscillation-type solutions [32]. The most distinctive signal expected in this case consists of solar anti-neutrinos, which would provide a clear signal in water Cerenkov experiments [34]. Moreover, for large enough neutrino mixing one expects also a sizeable suppression of the rates for pp neutrinos, potentially testable at the GNO experiment. Last but not least, the possible time dependence of the charged current signal due to solar cycles still remains as a possible tool to discriminate the MHD-model from the oscillation schemes.

Note added: As we finished our paper there appeared the paper E. K. Akhmedov and J. Pulido, hep-ph/0005173, which also considers predictions for some SNO observables in the conventional RSF scheme employing ad-hoc magnetic field profiles used in ref [14].

| Angular Range | Data _i $\pm \sigma_i$ |
|--------------------------------|----------------------------------|
| Day $0 < \cos \theta < 1$ | 0.463 ± 0.0115 |
| N1 $-0.2 < \cos \theta < 0$ | 0.512 ± 0.026 |
| N2 $-0.4 < \cos \theta < -0.2$ | 0.471 ± 0.025 |
| N3 $-0.6 < \cos \theta < -0.4$ | 0.506 ± 0.021 |
| N4 $-0.8 < \cos \theta < -0.6$ | 0.484 ± 0.023 |
| N5 $-1 < \cos \theta < -0.8$ | 0.478 ± 0.023 |

Table 6: Super-Kamiokande Collaboration zenith angle distribution of events [5].

A Zenith and Spectrum Data Samples and Fit Procedures

Here we summarize here the data used and the fit procedures adopted in this paper.

The zenith dependence data given by the Super-Kamiokande collaboration [5] are shown in table 6.

The recoil electron spectrum data are given as In table 7 $\sigma_{i,stat}$ is the statistical error, $\sigma_{i,exp}$ is the error due to correlated experimental errors, $\sigma_{i,cal}$ is the error due to the calculation of the expected spectrum, and $\sigma_{i,uncorr}$ is due to uncorrelated systematic errors.

In our study we use the experimental results from the Super-Kamiokande Collaboration on the recoil electron spectrum on the 18 energy bins including the results from the LE analysis for the 16 bins above 6.5 MeV and the results from the SLE analysis for the two low energy bins below 6.5 MeV, shown in table 7.

Notice that in table 7 we have symmetrized the errors to be included in our χ^2 analysis. We have explicitly checked that the exclusion region is very insensitive to this symmetrization. We define χ^2 for the spectrum as

$$\chi_S^2 = \sum_{i,j=1,18} (\alpha_{sp} \frac{R_i^{th}}{R_i^{\text{BP98}}} - R_i^{\text{exp}}) \sigma_{ij}^{-2} (\alpha_{sp} \frac{R_j^{th}}{R_j^{\text{BP98}}} - R_j^{\text{exp}}) \quad (19)$$

where

$$\sigma_{ij}^2 = \delta_{ij} (\sigma_{i,stat}^2 + \sigma_{i,uncorr}^2) + \sigma_{i,exp} \sigma_{j,exp} + \sigma_{i,cal} \sigma_{j,cal} \quad (20)$$

Again, we introduce a normalization factor α_{sp} in order to avoid double-counting with the data on the total event rate which is already included in χ_R^2 . Notice that in our definition of χ_S^2 we introduce the correlations amongst the different systematic errors in

| Energy bin | Data _i $\pm \sigma_{i,stat}$ | $\sigma_{i,exp}$ (%) | $\sigma_{i,cal}$ (%) | $\sigma_{i,uncorr}$ (%) |
|---------------------------|---|----------------------|----------------------|-------------------------|
| 5.5 MeV $< E_e <$ 6 MeV | 0.472 ± 0.037 | 1.3 | 0.3 | 4.0 |
| 6 MeV $< E_e <$ 6.5 MeV | 0.444 ± 0.025 | 1.3 | 0.3 | 2.5 |
| 6.5 MeV $< E_e <$ 7 MeV | 0.427 ± 0.022 | 1.3 | 0.3 | 1.7 |
| 7 MeV $< E_e <$ 7.5 MeV | 0.469 ± 0.022 | 1.3 | 0.5 | 1.7 |
| 7.5 MeV $< E_e <$ 8 MeV | 0.516 ± 0.022 | 1.5 | 0.7 | 1.7 |
| 8 MeV $< E_e <$ 8.5 MeV | 0.488 ± 0.025 | 1.8 | 0.9 | 1.7 |
| 8.5 MeV $< E_e <$ 9 MeV | 0.444 ± 0.025 | 2.2 | 1.1 | 1.7 |
| 9 MeV $< E_e <$ 9.5 MeV | 0.454 ± 0.025 | 2.5 | 1.4 | 1.7 |
| 9.5 MeV $< E_e <$ 10 MeV | 0.516 ± 0.029 | 2.9 | 1.7 | 1.7 |
| 10 MeV $< E_e <$ 10.5 MeV | 0.437 ± 0.030 | 3.3 | 2.0 | 1.7 |
| 10.5 MeV $< E_e <$ 11 MeV | 0.439 ± 0.032 | 3.8 | 2.3 | 1.7 |
| 11 MeV $< E_e <$ 11.5 MeV | 0.476 ± 0.035 | 4.3 | 2.6 | 1.7 |
| 11.5 MeV $< E_e <$ 12 MeV | 0.481 ± 0.039 | 4.8 | 3.0 | 1.7 |
| 12 MeV $< E_e <$ 12.5 MeV | 0.499 ± 0.044 | 5.3 | 3.4 | 1.7 |
| 12.5 MeV $< E_e <$ 13 MeV | 0.538 ± 0.054 | 6.0 | 3.8 | 1.7 |
| 13 MeV $< E_e <$ 13.5 MeV | 0.530 ± 0.069 | 6.6 | 4.3 | 1.7 |
| 13.5 MeV $< E_e <$ 14 MeV | 0.689 ± 0.092 | 7.3 | 4.7 | 1.7 |
| 14 MeV $< E_e <$ 20 MeV | 0.612 ± 0.077 | 9.2 | 5.8 | 1.7 |

Table 7: Recoil energy spectrum of solar neutrinos from the 825-day Super-Kamiokande Collaboration data sample [5].

the form of a non-diagonal error matrix in analogy to our previous analysis of the total rates. These correlations take into account the systematic uncertainties related to the absolute energy scale and energy resolution.

The general expression of the expected rate in the presence of oscillations R^{th} in a bin, is given from Eq.(18) but integrating within the corresponding electron recoil energy bin and taking into account that the finite energy resolution implies that the *measured* kinetic energy T of the scattered electron is distributed around the *true* kinetic energy T' according to a resolution function $Res(T, T')$ of the form

$$Res(T, T') = \frac{1}{\sqrt{2\pi}s} \exp \left[-\frac{(T - T')^2}{2s^2} \right], \quad (21)$$

where

$$s = s_0 \sqrt{T'/\text{MeV}}, \quad (22)$$

and $s_0 = 0.47$ MeV for Super-Kamiokande [4, 35]. On the other hand, the distribution of the true kinetic energy T' for an interacting neutrino of energy E_ν is dictated by the differential cross section $d\sigma_\alpha(E_\nu, T')/dT'$, that we take from [26]. The kinematic limits are

$$0 \leq T' \leq \bar{T}'(E_\nu), \quad \bar{T}'(E_\nu) = \frac{E_\nu}{1 + m_e/2E_\nu}. \quad (23)$$

For assigned values of s_0 , T_{\min} , and T_{\max} , the corrected cross section $\sigma_\alpha(E)$ ($\alpha = e, x$) is given as

$$\sigma_\alpha(E_\nu) = \int_{T_{\min}}^{T_{\max}} dT \int_0^{\bar{T}'(E_\nu)} dT' Res(T, T') \frac{d\sigma_\alpha(E_\nu, T')}{dT'}. \quad (24)$$

Acknowledgements

We thank Alexei Bykov, Vladimir Kutvitsky, Dmitri Sokoloff and Victor Popov for useful discussions. This work was supported by DGICYT grant PB98-0693, by the European Commission under Intas Project 96-0659 and TMR contract ERBFMRX-CT96-0090, and by an Iberdrola research excellence grant. VBS and TIR were partially supported by the RFBR grant 00-02-16271 and OGM was supported by the CONACyT-Mexico grant J32220-E.

References

- [1] R. Davis, Jr, D. S. Harmer, and K. C. Hoffman, Phys. Rev. Lett. **20**, (1968) 1205; B. T. Cleveland *et al.*, Ap. J. **496**, 505 (1998).
- [2] T. Kirsten, Talk at the Sixth international workshop on topics in astroparticle and underground physics September, TAUP99, Paris, September 1999.
- [3] SAGE Collaboration, V. N. Gavrin *et al.*, Talk at the XVIII International Conference on Neutrino Physics and Astrophysics, 4-9 June 1998, to be published in Nucl. Phys. B (Proc. Suppl.).
- [4] Super-Kamiokande Collaboration, Y. Fukuda *et al.*, Phys. Rev. Lett. **82**, 1810 (1999); The SK-collaboration, Phys. Rev. Lett. 82 (1999) 2430, Fukuda et al, hep-ex/9812011
- [5] Y. Suzuki, talk a the “XIX International Symposium on Lepton and Photon Interactions at High Energies”, Stanford University, August 9-14, 1999; M. Nakahata, talk at the “6th International Workshop on Topics in Astroparticle and Underground Physics, TAUP99”, Paris, September 1999.
- [6] G. Fiorentini and B. Ricci, proceedings of International Workshop on Physics Beyond the Standard Model: From Theory to Experiment (Valencia 97), Valencia, Spain, 13-17 Oct 1997, Ed. I. Antoniadis, L. Ibanez, J. W. F. Valle, World Scientific Publishing Co., 1998, ISBN 981-02-3638-7, pages 241-259.
- [7] Y. Fukuda *et al.* [Super-Kamiokande Collaboration], Phys. Rev. Lett. **81** (1998) 1562 [hep-ex/9807003]; see also Phys. Lett. **B433** (1998) 9 [hep-ex/9803006] and Phys. Lett. **B436** (1998) 33 [hep-ex/9805006]. For an updated global analysis of the atmospheric neutrino data in terms of neutrino oscillations see N. Fornengo, M. C. Gonzalez-Garcia and J. W. F. Valle, hep-ph/0002147, to be published in Nucl. Phys. **B** (2000).
- [8] S.P. Mikheev, A.Yu. Smirnov, Sov. J. Nucl. Phys. 42 (1985) 913; Nuovo Cimento C9 (1986) 17; L. Wolfenstein, Phys. Rev. D17 (1978) 2369.
- [9] J. Schechter and J. W. F. Valle, Phys. Rev. **D24** (1981) 1883; Erratum-ibid. **D25** (1982) 283
- [10] J. Schechter and J. W. F. Valle, Phys. Rev. **D22** (1980) 2227.

- [11] E. Kh. Akhmedov, Phys. Lett. B 213 (1988) 64; C.-S. Lim and W.J. Marciano, Phys. Rev. D 37 (1988) 1368. For a review see E.Kh. Akhmedov, *The neutrino magnetic moment and time variations of the solar neutrino flux*, Preprint IC/97/49, Invited talk given at the 4-th International Solar Neutrino Conference, Heidelberg, Germany, April 8-11, 1997.
- [12] S. Bergmann, M. M. Guzzo, P. C. de Holanda, P. I. Krastev and H. Nunokawa, hep-ph/0004049.
- [13] J. W. F. Valle, Phys. Lett. **B199** (1987) 432.
- [14] M.M. Guzzo and H. Nunokawa, Astropart. Phys. **11** (1999) 317; J. Pulido, E.K. Akhmedov, hep-ph/9907399.
- [15] J. Derkaoui, Y. Tayalati hep-ph/9909512.
- [16] H. Yoshimura, Astrophys. J., **178** (1972) 863; Astrophys. J. Suppl. Ser., **52** (1983) 363; M. Stix, Astron. & Astrophys. **47** (1976) 243; Ya. B. Zeldovich, A. A. Ruzmaikin and D.D. Sokoloff, *Magnetic Fields in Astrophysics*, Gordon and Breach Science Publishers, 1983 and references therein.
- [17] V. A. Kuvitskii, L.S. Solov'ev, JETP, **78** (1994) 456.
- [18] E.N. Parker, *Cosmological Magnetic Fields*, Oxford University Press, Oxford, 1979; E.N. Parker, Astrophys. J., 408 (1993) 707
- [19] F. Moreno-Insertis, Astron. & Astrophys, **166** (1986) 291
- [20] C. Azneziris and J. Schechter, Phys. Rev. **D45** (1992) 1053; C. Azneziris and J. Schechter, IJMP, **A6** (1991) 2375; E. Kh. Akhmedov, S. T. Petcov and A. Yu. Smirnov, Phys. Rev. **D48** (1993) 2167; A. B. Balantekin ahd F. Loret, Phys. Rev. **D48** (1993) 5496; T. Kubota, T. Kurimoto, M. Osura, E. Takasugi, Phys. Lett. B292 (1992) 195.
- [21] S. Chandrasekar and E. Fermi, Astrophys. J., 118 (1953) 116.
- [22] W. Dziembowski, G. Fiorentini, B. Ricci, R. Sienkiewicz, A&A, 343, 990 (1999); J. Bahcall, M. Pinsonneault, Reviews of Modern Physics, **67**, 781-808 (1995).
- [23] J.N. Bahcall, S. Basu and M. Pinsonneault, Phys. Lett. B433 (1998) 1.

- [24] M. C. Gonzalez-Garcia, P. C. de Holanda, C. Pena-Garay and J. W. F. Valle, Nucl. Phys. **B573** (2000) 3 [hep-ph/9906469].
- [25] J. N. Bahcall, E. Lisi, D. E. Alburger, L. De Braeckeleer, S. J. Freedman, and J. Napolitano, Phys. Rev. **C54**, 411 (1996).
- [26] J. N. Bahcall, M. Kamionkowsky, and A. Sirlin, Phys. Rev. **D51**, 6146 (1995).
- [27] Bahcall's Home Page, <http://www.sns.ias.edu/~jnb/SNdata>
- [28] M. C. Gonzalez-Garcia and C. Pena-Garay, hep-ph/0002186, to appear in Phys. Rev. **D**.
- [29] C. Giunti, M. C. Gonzalez-Garcia and C. Pena-Garay, hep-ph/0001101, to appear in Phys. Rev. **D**.
- [30] For SNO predictions in neutrino oscillation models see J. N. Bahcall, P. I. Krastev and A. Y. Smirnov, hep-ph/0002293 and Phys. Lett. **B477** (2000) 401.
- [31] K. Kubodera, S. Nozawa, Int. J. Mod. Phys. E 3 (1994) 101; K. Kubodera's home-page, <http://nuc003.psc.sc.edu/~kubodera/>.
- [32] O. Miranda et al, in preparation.
- [33] P. C. de Holanda, C. Pena-Garay, M. C. Gonzalez-Garcia and J. W. F. Valle, Phys. Rev. **D60** (1999) 093010 [hep-ph/9903473].
- [34] G. Fiorentini, M. Moretti and F. L. Villante, Prog. Part. Nucl. Phys. **40** (1998) 149.
- [35] B. Faïd, G. L. Fogli, E. Lisi and D. Montanino, Phys. Rev. **D55**, 1353 (1997).